



One-pot hydrothermal synthesis of highly efficient $\text{SnO}_x/\text{Zn}_2\text{SnO}_4$ composite photocatalyst for the degradation of methyl orange and gaseous benzene



Jinghui Wang^a, Hui Li^a, Sugang Meng^a, Li Zhang^a, Xianliang Fu^{a,*}, Shifu Chen^{a,b,*}

^a College of Chemistry and Material Science, HuaiBei Normal University, HuaiBei, Anhui 235000, China

^b Department of Chemistry, Anhui Science and Technology University, Fengyang, Anhui 233100, China

ARTICLE INFO

Article history:

Received 9 March 2016

Received in revised form 21 June 2016

Accepted 28 June 2016

Available online 28 June 2016

Keywords:

Photocatalysis

$\text{SnO}_x/\text{Zn}_2\text{SnO}_4$

Heterojunction

Benzene degradation

ABSTRACT

Zn_2SnO_4 (ZTO) based composites have a promising application in photocatalysis. Developing a facile route to prepare high performance ZTO based photocatalyst is still required. A one-pot hydrothermal method was developed in this work to prepare SnO_x/ZTO (SZTO-H) for the first time. Several characterization techniques were used to investigate its composition, structure, optical property, and morphology. The results indicated that SnO_x component is SnO_2 accompanied by a trace amount of Sn_2O_3 . A type-II heterojunction is formed at the interface of SnO_x and ZTO, which leads to a wide separation of photo-induced electrons (e^-) and holes (h^+). Thus, compared to pristine SnO_2 and ZTO, a higher and more stable photocatalytic activity was observed on SZTO-H. Although similar SnO_2/ZTO composites could be prepared by solid-state reaction routes (SSRs), their activities are substantially lower than SZTO-H as the surface areas were significantly reduced and some surface defects were introduced. The photocatalytic performance of SZTO-H is even superior to P25. Besides ZTO, we believe that the developed synthesis strategy is also applicable to the preparation of other ternary oxides based composites like $\text{SnO}_x/\text{ZnGa}_2\text{O}_4$ and $\text{SnO}_2/\text{Mg}_2\text{SnO}_4$.

© 2016 Elsevier B.V. All rights reserved.

1. Introduction

Due to its high electrical conductivity, chemical stability, and attractive optical properties, the n type ternary semiconductor Zn_2SnO_4 (ZTO) has shown some promising applications in dye-sensitized solar cells, gas sensor, Li-ion battery, and photocatalysis [1–6]. The most attractive application is in photocatalysis for solar energy conversion and environmental remediation due to the unique merits of the technology in greenness and sustainability.

The versatility of ZTO in photocatalysis has been extensively confirmed by the degradation of dyes, benzene, evolution of H_2 from ethanol solution, and reduction of CO_2 to CH_4 [7–16]. The activities can be optimized by controlling ZTO size, morphology, and structure, which are commonly achieved by adopting a proper preparation method. Including thermal evaporation, calcination, sol-gel synthesis, mechanical grinding, and hydrothermal reaction

have been developed to prepare ZTO [1,6,11,15,17–25]. Among them, the facile hydrothermal method [1,6,11,18,20,25] was preferred to prepare well-crystallized and phase-pure ZTO which is difficult to be obtained by conventional solid-state reaction route (SSR) due to the evaporation of ZnO at a high temperature [26]. Besides, ZTO size and morphology also can be controlled by varying the additives and the hydrothermal temperature or time. Including cubes, spheres, rods, and tubes-like ZTO have been successfully prepared by hydrothermal method [25,27,28]. As for the structure, ZTO can be present in a normal or inverse spinel structure which can be briefly described as $(\text{Sn}_{1-x}\text{Zn}_x)_{\text{tetra}}[\text{Sn}_x\text{Zn}_{2-x}]_{\text{octa}}\text{O}_4$ [29]. The value of x stands for the degree of the inversion and it ranges from 0 to 1 which indicates the normal and inverse spinel, respectively. The inverse-spinel structure is the thermodynamically stable configuration and could be readily prepared by hydrothermal method [1,6]. In a word, the hydrothermal reaction is an ideal route to synthesize ZTO and optimize its photocatalytic performance.

The photocatalytic activity of ZTO is restricted by the fast recombination of photo-induced electron-hole pairs (e^- , h^+) [30]. Besides optimal the structure and morphology feature of ZTO, another pathway to improve the activity of ZTO is to couple it with a semi-

* Corresponding authors at: College of Chemistry and Material Science, HuaiBei Normal University, HuaiBei, Anhui 235000, China

E-mail addresses: fuxiliang@gmail.com (X. Fu), chshifu@chnu.edu.cn (S. Chen).

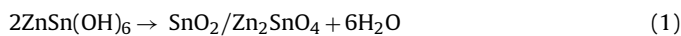
conductor that possesses a different band structure to that of ZTO. Some heterojunctions then can be constructed in the composite, which can promote the separation of e^- and h^+ and extend the absorption range. This strategy is more effective than the doping process to improve the photocatalytic performance as the formation of mid-gap or vacancy states can be largely avoided. The literatures indicated that ZTO could be coupled with WO_3 , Fe_2O_3 , ZnO , SnO_2 , $g-C_3N_4$, and $BiOI$ and the resulted composites showed enhanced sensor, electrical, or photovoltaic responses [9,13,31–36], as well as the photocatalytic activity [13,30,34,35]. Moreover, the activity could be even extended to the visible light region by coupling with some narrow bandgap semiconductors like $g-C_3N_4$ and $BiOI$ [7,8]. Unfortunately, these ZTO composites were generally prepared by a harsh or a sophisticated two-step process. Taking the most studied SnO_2/ZTO (SZTO) as example, it is commonly prepared by sintering of SnO_2 and ZnO mixture at *ca.* 1000 °C [32,37] or thermal treatment of $ZnSn(OH)_6$ precursor at an elevated temperature [9,33,36]. The high temperature results in a reduction of the surface area and the formation of some surface defects like the oxygen vacancies [9,37–39] or Zn interstitials [9,40]. The photocatalytic activity of the composites will be unfavored by these preparation routes as a low surface area sample was resulted and excessive lattice defects were introduced. Therefore, developing a facile route to prepare ZTO based composites with a high activity is still required.

Herein, we developed a facile one-pot hydrothermal method to fabricate SnO_x/ZTO composite photocatalyst (SnO_x refers to SnO_2 accompanied by a trace amount of Sn_2O_3). The results indicated that a type-II heterojunction can be formed at the interface of SnO_x and ZTO. The prepared SnO_x/ZTO showed higher activity than the samples prepared by conventional SSRs for the degradation of methyl orange (MO) and gaseous benzene (C_6H_6). A possible mechanism for the enhanced and stable activity was finally proposed and discussed based on the characterization results.

2. Experimental

2.1. Materials preparation and characterization

All chemicals were analytical grade and used as received. $Na_2SnO_3 \cdot 4H_2O$, $ZnCl_2$, MO, and terephthalic acid (TA) were provided by Sinopharm Chemical Reagent Co., China. Commercial ZnO and SnO_2 were purchased from Alading Reagent Co., Shanghai, China. SnO_x/Zn_2SnO_4 (denoted as SZTO-H) was prepared by a one-pot hydrothermal method. 40 mL 0.1 M $ZnCl_2$ solution was first introduced into a 100 mL PTFE vessel. 40 mL 0.1 M Na_2SnO_3 was then added dropwise to the solution under vigorous stirring. The resultant white slurry (*ca.* 80 mL) was transferred into an autoclave and kept in an oven at 180 °C for 24 h. The solid product formed after the treatment was collected by centrifugation, rinsed thoroughly with deionized water, and finally dried in air at 120 °C for 4 h. For comparison, the conventional SSRs [9,15,33,41] were used to prepare SZTO with $ZnSn(OH)_6$ (ZHS) and a mixture of ZnO and SnO_2 as a precursor, respectively. ZHS was prepared by a hydrothermal method according to the reported procedure [42]. SnO_2/ZTO (denoted as SZTO-H-S) then could be obtained by annealing ZHS at 800 °C for 2 h via the reaction of Eq. (1). In another SSR, a mixture of stoichiometric ZnO (1.02 g) and SnO_2 (1.90 g) was first pressed into pellets, followed by a calcination treatment in air at 1100 °C for 2 h. SnO_2/ZTO can be produced via Eq. (2). The resulted sample was finally ground into powders (denoted as SZTO-S). The ramping rate of the SSRs was 3 °C/min. Pristine ZTO was prepared by the reported hydrothermal process [6,12].



X-ray diffraction (XRD) patterns of the prepared samples were recorded on a Bruker D8 Advance diffractometer with $Cu K\alpha$ radiation $\lambda = 1.5406 \text{ \AA}$. UV-vis diffuse reflectance spectra (UV-vis DRS) were measured on a UV-vis-NIR spectrophotometer (Shimadzu UV 3600) with $BaSO_4$ as a reference. The morphology of the sample was examined by using a field emission scanning electron microscopy (SEM, FEI Nova NanoSEM 230) and a transmission electron microscopy (TEM, FEI Tecnai G2 F20 S-TWIN), respectively. The composition of the prepared SZTO-H was investigated by an energy-dispersive X-ray spectrometer (EDS) attached to the SEM instrument. N_2 adsorption–desorption isotherms were obtained at 77 K by using a Micromeritics Tristar II 3020 surface area analyzer. Multipoint Brunauer–Emmett–Teller (BET) specific surface areas were calculated according to the BET transformation of the adsorption isotherms. X-ray photoelectron spectroscopy (XPS) analysis was conducted on an ESCALAB 250 photoelectron spectrometer (Thermo Fisher Scientific) at $3.0 \times 10^{-10} \text{ mbar}$ by using $Al K\alpha$ X-ray beam (1486.6 eV). All binding energies were calibrated to the C 1s peak at 284.6 eV.

Photoelectric current responses of the samples were recorded on a CHI 660E electrochemical workstation (Chenhua, Shanghai) at a bias of -0.2 V in a standard three-electrode cell with the samples as the working electrode, an $Ag/AgCl$ electrode (in 3 M KCl solution) as the reference electrode, and a Pt plate as the counter electrode, respectively. 0.2 M Na_2SO_4 aqueous solution was used as the electrolyte. The film working electrodes (exposed area $0.6 \times 0.6 \text{ cm}^2$) were prepared by drop-casting samples/ethanol suspensions onto FTO glass substrates followed by drying the film at 60 °C overnight to improve adhesion. A UV lamp (TUV 6W/G6 T5, Philips) with a monochromatic emission at 254 nm was used as the light source and the irradiation was chopped manually every *ca.* 10 s during the measurements. The Mott–Schottky plots were obtained by measuring the electrochemical impedance spectra to evaluate the flat-band potential of SnO_2 and ZTO. The measurements were conducted on the same electrochemical workstation in the standard three-electrode cell. A 0.2 M Na_2SO_4 aqueous solution was used as the electrolyte (the pH is *ca.* 7.0) and then purged with N_2 before the measurement. The potential ranged from -0.8 to 0.6 V (vs $Ag/AgCl$) at a fixed frequency of 1.25 KHz.

The formation of hydroxyl radicals ($\bullet OH$) in the suspension of prepared samples was studied by photoluminescence (PL) technique by using TA as a probe molecule [43]. TA reacts readily with $\bullet OH$ to produce a highly fluorescent product of 2-hydroxyterephthalic acid (TAOH) which has a maximum fluorescence peak located at *ca.* 425 nm. The determined procedure was similar to the degradation of MO (see Section 2.2) except the MO solution was replaced by an aqueous solution of $5 \times 10^{-4} \text{ M}$ TA and $2 \times 10^{-3} \text{ M}$ NaOH. During irradiation, 3 mL of the suspension was collected with a pipette every 5 min and then centrifuged and filtrated. The fluorescence signal of TAOH in the clear solution was measured by a fluorescence spectrophotometer (JASCO FP-6500) at room temperature.

2.2. Photocatalytic activity

The photocatalytic activity of the prepared samples was evaluated by the degradation of MO solution and gaseous C_6H_6 , respectively. The schematic diagram of the reaction systems had been described in our former works [44]. The decoloration of MO was carried out in a tubular reactor which was surrounded by a water cooling jacket. The solution temperature was controlled at 20 °C by a Julabo F12 cooling bath (Julabo Labortechnik, Germany). A 9 W H-shaped low pressure mercury UV lamp (Philips TUV PLS-9W, with a monochromatic emission at 254 nm) was assembled at

the center of the tubular reactor. In a typical run, 0.1 g photocatalyst was first dispersed in 200 mL 20 ppm MO aqueous solution and then stirred in dark for 30 min to establish an adsorption-desorption equilibrium. After that, the UV-vis absorption spectrum of the supernatant was measured as the initial concentration of MO (C_0). During irradiation, a 3 mL solution was sampled at various illumination time intervals followed by a centrifugation at 9000 rpm for 3 min. The residual concentration of MO in the filtrate was analyzed by using UV-vis spectrophotometer (Persee TU-1950). The solution was continuously ventilated with air at a rate of 20 mL/min throughout the whole reaction.

Photocatalytic degradation of gaseous C_6H_6 was performed in a continuous flow mode in a plug flow micro-reactor made of quartz tube (with length of 250 mm, and inner diameter of 4 mm). The reactor was surrounded by four 6 W UV lamps (TUV 6W/G6 T5, Philips, with a monochromatic emission at 254 nm). The heat generated by the lamps was removed by a suction fan. The reactor temperature was controlled at *ca.* 30 °C. In a typical experiment, 0.1 g sample was first mixed thoroughly with 1.0 g 50–70 mesh high purity quartz sands (as a support). The mixture was then loaded into the reactor. A constant concentration of benzene vapor (250 ppm with the balance of O_2) was supplied by a gas cylinder (supplied by Dalian Da'te gas Co. China). The flow rate was kept at 30 mL/min corresponding to a reactor residence time of 1.8 s (calculated based on the volume of the photocatalyst and the velocity of the feed gas). Simultaneous determination of the residual C_6H_6 and the product of CO_2 were performed on an online GC (Agilent 7820A) with FID and TCD, respectively. The conversion (C%) and the mineralization efficiency (M%) of C_6H_6 were calculated according to the steady-state reaction data by Eq. (3) and Eq. (4), respectively. It should be noted that the calculation of M% is based on the converted C_6H_6 amount, not the feeding C_6H_6 amount. The mineralization rate (r_M) of C_6H_6 was calculated by Eq. (5). The feeding gas was treated as an ideal gas for the calculations.

$$C\% = \frac{[C_6H_6]_{initial} - [C_6H_6]_{steady}}{[C_6H_6]_{initial}} \quad (3)$$

$$M\% = \frac{[CO_2]_{steady}}{([C_6H_6]_{initial} - [C_6H_6]_{steady}) \times 6} \quad (4)$$

$$r_M = \frac{[C_6H_6]_{initial} \times 30(\text{mL}/\text{min}) \times 60(\text{min}) \times C\%}{22.4(\text{L/mol}) \times 0.1(\text{g})} \times M\% \quad (5)$$

3. Results and discussion

3.1. XRD analysis

The XRD patterns of the prepared SZTO samples, ZTO, and the commercial SnO_2 are shown in Fig. 1. It indicates that pure ZTO was successfully synthesized. The diffraction peaks (Fig. 1a) can be indexed to inverse-spinel ZTO with a cubic phase structure. In general, two sets of diffraction peaks which are originated from cubic ZTO (JCPDS card: 74-2184) and rutile-type tetragonal SnO_2 (JCPDS card: 77-449) can be found in the SZTO spectra (Fig. 1b), suggesting that the formation of SnO_2/Zn_2SnO_4 composites. In addition, three weak diffraction peaks of triclinic Sn_2O_3 (JCPDS card: 25-1259) located at $2\theta = 39.3, 50.1, 52.6^\circ$ can be observed in SZTO-H. This sub-valent tin oxides species is a sum of independent SnO_2 and SnO crystals [45,46] and is more likely formed by the etching of lattice O atoms via Eq. (6) [47] under the hydrothermal condition. However, this component cannot be perceived in the other two samples prepared by the SSRs. The strong diffraction peaks of SZTO-H and SZTO-S suggest that the samples are well crystallized. Comparison test indicated that the preparation of SZTO-S requires the temperature as high as 1100 °C (Fig. S1). As shown in Fig. S2a, the XRD pattern of the prepared ZHS which was used as a precur-

sor for SZTO can be ascribed to cubic phase $ZnSn(OH)_6$ (JCPDS No. 073-2384). As Zn^{2+} and Sn^{4+} are dispersed at molecular level in ZHS, the conversion of ZHS to SZTO is more readily than from the mixture of ZnO and SnO_2 [9]. SZTO-H-S can be successfully prepared at 800 °C (Fig. S2c) and the diffraction peaks are quite weaker and broader than that of SZTO-S. A similar phenomenon has been observed [9,36].



Besides the prepared ZTO, commercial SnO_2 was also used as a reference component to compare the photocatalytic performance of SZTO samples. The choice was based on two considerations. First, as shown in Fig. 1c, the commercial SnO_2 has a tetragonal structure and is well crystallized. Its diffraction pattern resembles that of the SnO_2 component in SZTO-H, which indicates their similarity to a certain extent. Second, the commercial SnO_2 has been used as a precursor for the synthesis of SZTO-S.

3.2. UV-visible absorption

UV-vis DRS is a useful technique to study the electronic state information of a photocatalyst. Fig. 2 shows the UV-vis DRS of the prepared SZTO samples and the pristine ZTO and SnO_2 . It indicates that the intrinsic band gap (BG) transition of SZTO-H and ZTO locates at almost the same wavelength of 350 nm, corresponding to a band gap energy (E_g) of 3.5 eV (calculated by $1240/\lambda_g$, where λ_g is the threshold of the band gap absorption). Compared with SZTO-H, the BG absorption edges of the SZTO samples prepared by SSRs (i.e. SZTO-H-S, and SZTO-S) have a slight red-shift to *ca.* 390 nm, corresponding to an E_g of 3.2 eV. The absorptions of the prepared SZTO samples should be the superposition of the transition of SnO_2 and ZTO. It has been reported that an apparent red-shift of ZTO spectrum could occur with the annealing temperature due to the changes of the ZTO grain sizes and the lattice constant [28]. Thus, the observed red-shift of SZTO samples may be caused by ZTO component. Furthermore, a sub-absorption can be found in SZTO-S in the visible light region (highlighted by gray shading in Fig. 2), which may be contributed by some surface defects like the oxygen vacancies or Zn interstitials formed at 1100 °C [9,37–41]. Unlike SZTO-S, the sub-absorption cannot be found in SZTO-H-S prepared at 800 °C suggesting that the surface defects are favored at a high calcination temperature. The commercial SnO_2 prepared by an aerosol pyrolysis process also exhibits similar sub-absorption in addition to the BG absorption (threshold at 370 nm). It seems that the oxygen vacancy may locate in SnO_2 component, which was caused by the high calcination temperature. For SZTO-H and ZTO prepared by hydrothermal method, no similar sub-absorption can be found in the spectra. The formation of the vacancy defects can be avoided by hydrothermal process. Reported works [46,48,49] indicated that heterovalent tin oxides like Sn_2O_3 and Sn_3O_4 exhibit a narrower band lower than 2.7 eV. Although triclinic Sn_2O_3 has been confirmed by XRD in SZTO-H (Fig. 1b), no similar absorption was observed suggesting that the Sn_2O_3 component may stay in SnO_2 bulk rather than on the surface. In this case, the Sn_2O_3 absorption cannot be detected by UV-vis DRS, a typical surface analysis technology. The real E_g of ZTO is still controversial and the reported values are ranging from 3.2 to 3.9 eV [27,28]. As the E_g of SnO_2 (3.4 eV) is close to that of ZTO [9], the observed BG energies of the prepared SZTO samples also fall within the range.

The E_g values of the prepared samples were further determined by the Tauc plot approach [50]: $K(hv - E_g)^{1/n} = F(R)hv$, where $F(R)$ is the absorption coefficient converted from R% to F(R) by using the Kubelka–Munk method, hv is photon energy, K is a constant, and n equals 2 for direct transition of SnO_2 [51] and ZTO [26,27,40]. The plots are shown in the inset of Fig. 2. The estimated E_g values of the samples are slightly higher (*ca.* 0.1 eV) than the results calculated

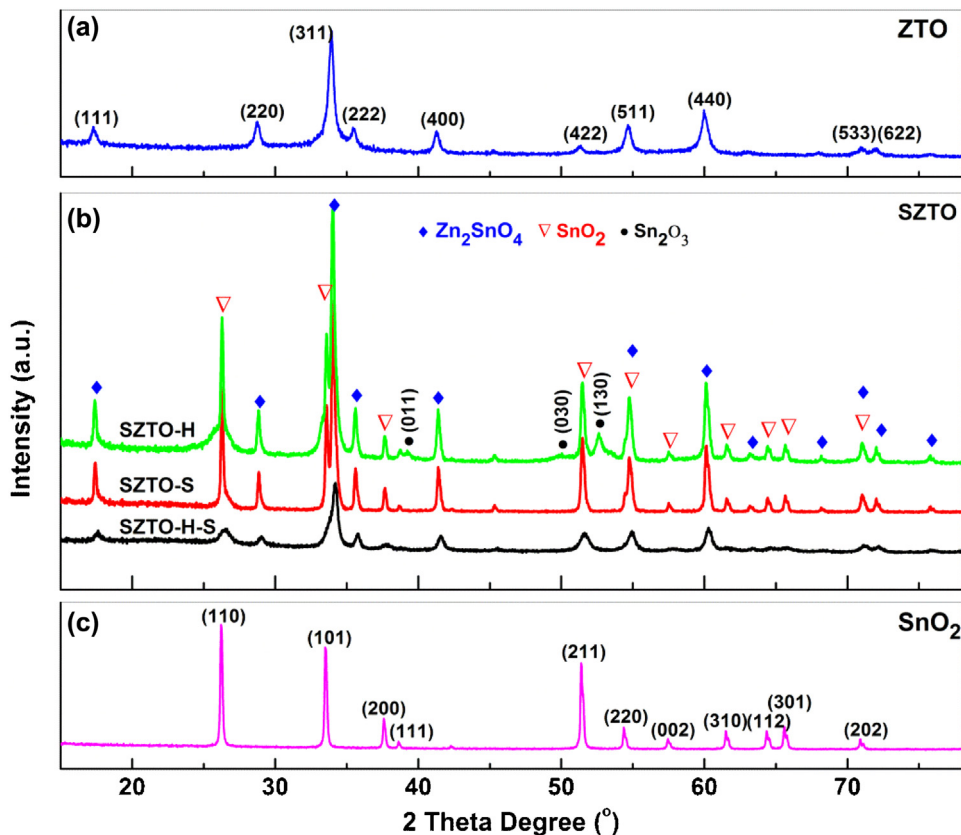


Fig. 1. XRD patterns of the prepared (a) ZTO, (b) SZTO samples, and (c) the commercial SnO₂.

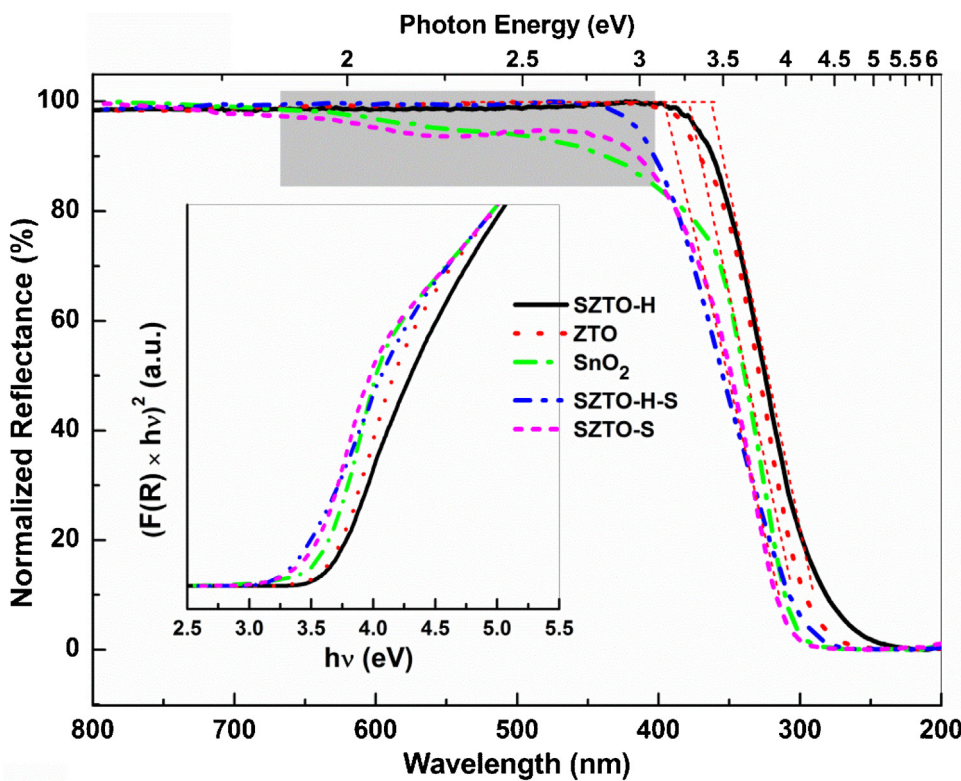


Fig. 2. UV-vis DRS patterns of the prepared ZTO, SZTO, and commercial SnO₂. The inset shows the corresponding Tauc plots.

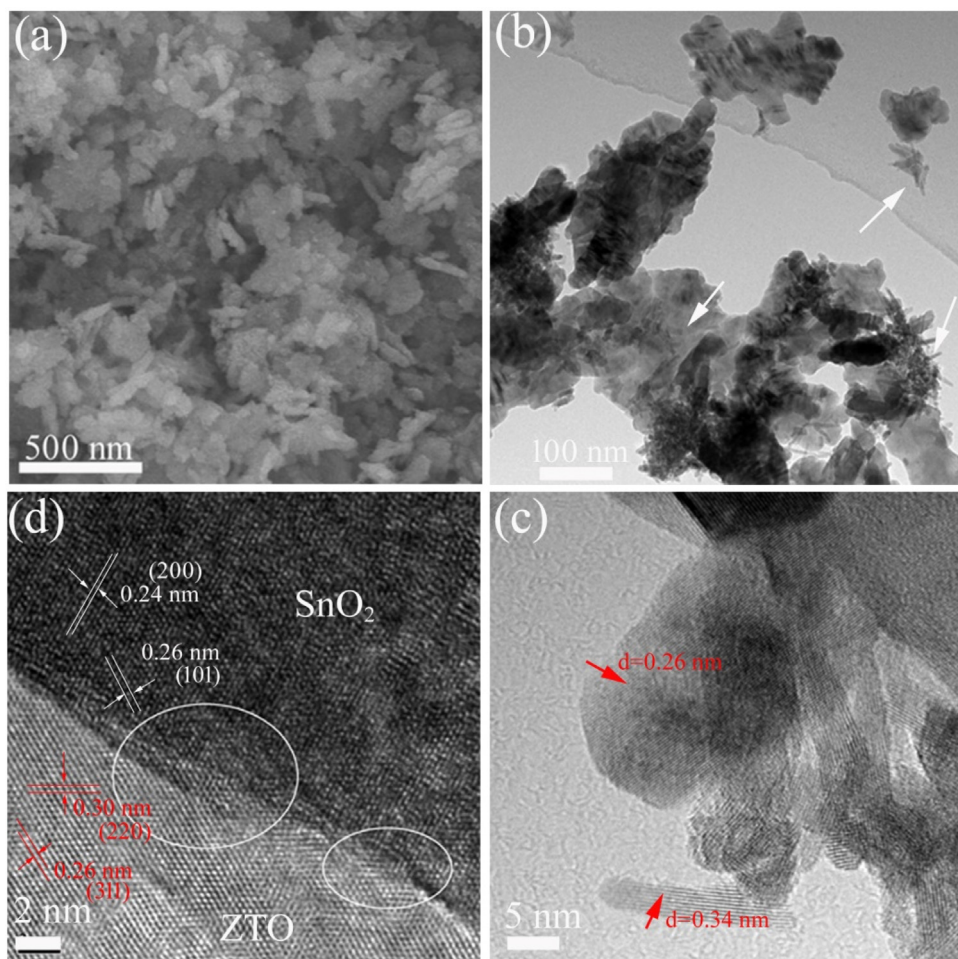


Fig. 3. (a) SEM, and (b–d) H/TEM images of the prepared S-ZTO-H.

Table 1

Summarize the preparation, characterization, and photocatalytic activity results of the prepared samples and the commercial SnO_2 and P25.

Sample notation	Preparation route	E_g (eV)	BET (m^2/g)	Photocatalytic activity				
				MO	$C_6\text{H}_6$	k^a	$C\%$	$M\%$
				C_6H_6	C_6H_6			
SZTO-H	one-pot hydrothermal	3.5	21.7	83.4	23.7	80.3	38.3	
SZTO-H-S	hydrothermal & SSR	3.2	10.5	19.2	6.7	79.3	10.7	
SZTO-S	SSR	3.2	1.0	9.3	3.5	94.8	6.7	
ZTO ^c	hydrothermal	3.5	22.0	69.7	51.8	60.4	62.9	
SnO_2	Commercial product	3.3	1.2	6.1	4.8	92	8.9	
P25 ^c	Commercial product	3.0	ca. 50.0	76.4	9.6	88.5	17.1	

^a $\times 10^{-3} \text{ min}^{-1}$.

^b $\text{umol h}^{-1} \text{ g}^{-1}$.

^c Unstable for the abatement of benzene, the average data was used for the calculations.

by $1240/\lambda_g$. Here, the results measured by $1240/\lambda_g$ are summarized in Table 1 for easy reference and are used for the subsequent discussion.

3.3. Morphology and XPS analysis

The morphology of SZTO-H was characterized by SEM and TEM. SEM image (Fig. 3a) reveals that the sample is composed of rods and flakes-like particles. The morphology feature can be further corroborated by the TEM image. As indicated by the arrows in Fig. 3b, the flakes are decorated by some aggregated nano-rods with a diameter of ca. 5 nm and a length no more than 100 nm. As the electron beam readily penetrates the flakes, a bright contrast can be found between the flakes and the rods. Fig. 3c shows the HRTEM image of the composites. The well-resolved lattice fringes of 0.34 and 0.26 nm can be observed on the rod and flake which correspond to the (110) planes of rutile SnO_2 and the (311) planes of spinel ZTO, respectively. A further HRTEM analysis around the interface area with different bright contrast was specially performed. As shown in Fig. 3d, another two lattice fringes with d values of 0.24 and 0.26 nm can be found in the dark area, which correspond to SnO_2 (200) and (101) planes, respectively. In the bright area, two sets of lattice fringes with d values of 0.26 and 0.30 nm can be observed, which match well with the (311) and (220) interplanar distance of ZTO, respectively. As no lattice mismatch exists between SnO_2 (101) and ZTO (311) planes, some intersections of the lattice fringes can be found in Fig. 3d (indicated by the circles) suggesting an intimate contact is formed between SnO_2 and ZTO. Thus, the formation of a heterojunction at the interfaces of SnO_2 and ZTO can be expected, which has a potential function to promote the separation of photo-induced e^- and h^+ . Although the Sn_2O_3 diffraction peaks have been disclosed in the XRD pattern (Fig. 1b), the component is still difficult to be distinguished by the SEM and TEM images. EDS analysis (Fig. S3) indicates that the main ingredients of SZTO-H are Sn, Zn and O besides C and Au, which come from the graphite conductive adhesive and Au spraying, respectively. Thirteen points located at different place were taken for the measurements and the average atomic ratio of Sn:Zn:O is 20.1%:20%:59.9%, which is almost identical to the theoretical value of SZTO (20%:20%:60%).

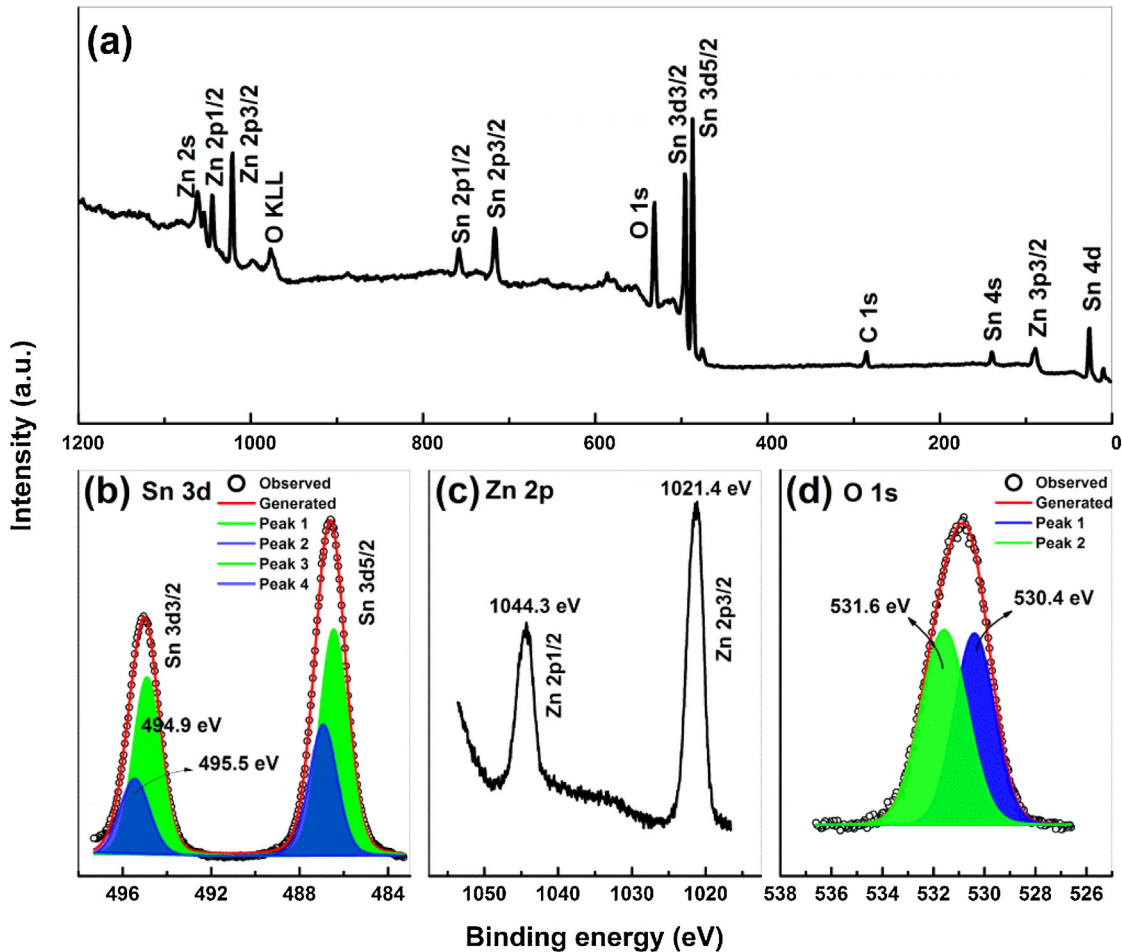


Fig. 4. (a) survey and high resolution XPS spectra of (b) Zn 2p, (c) Sn 3d, and (d) O 1s of the prepared SZTO-H.

The surface composition and the oxidation state of the constituent elements in SZTO-H were studied by XPS. Besides the adventitious carbon, the survey XPS spectrum (Fig. 4) reveals that the sample is composed of Sn, Zn, and O. High resolution XPS spectra of the Sn 3d, Zn 2p, and O 1s elements are shown in Fig. 4b–d. The double peaks located at 495 and 486.6 eV in Fig. 4b can be ascribed to the binding energy of Sn 3d_{3/2} and 3d_{5/2}, respectively. The Sn 3d spectrum can be further deconvoluted into two sets of peaks centered at (494.9, 486.4) and (495.5, 486.9) eV with a spin-orbit splitting energy of ca. 8.5 eV. They can be attributed to the chemical state of Sn²⁺ (in Sn₂O₃) and Sn⁴⁺, respectively [48,52]. As the detection depth of XPS with an Al target can reach 5 nm, the Sn₂O₃ confined in the interior of SnO₂ nano-rods can be distinguished by XPS. For Zn 2p spectrum (Fig. 4c), the peaks appeared at 1044.3 and 1021.4 eV correspond to Zn 2p_{1/2} and 2p_{3/2} of Zn²⁺ state in ZTO [7,53]. The O 1s peak (Fig. 4d) can be deconvoluted into two peaks with binding energy of 531.6 and 530.4 eV. The peak at 531.6 eV can be ascribed to surface O species like –OH or the coordination of O in Sn–O–Zn, while the other one at 530.4 eV can be attributed to the lattice O in Sn–O–Sn [54–57]. The ratio of Sn, Zn, and O in SZTO-H was determined by the XPS peak areas after correction of the sensitivity factors of the elements and the result (Sn:Zn:O) is 20.1%: 19.3%: 60.6%, in agreement with the EDS result. A slight high Sn concentration is observed implying the enrichment of surface tin oxide species. A similar phenomenon has been reported in SnO_x/ZnGa₂O₄ [58].

3.4. Photocatalytic activity

The photocatalytic activity of the prepared SZTO samples was first evaluated by the degradation of MO solution. For comparison, the activities of pristine SnO₂, ZTO, and Degussa P25 (TiO₂) were also investigated under the same conditions. The variation of the absorption spectra of MO solution with the irradiation time is shown in Fig. S4. The temporal changes of MO concentration are compared in Fig. 5. A decay of MO absorption can be observed for all tests, even the test without photocatalyst (Fig. S4a). The high energy UVC irradiation (254 nm) accounts for the photolysis of MO [42,44]. Among the samples, SZTO-H shows the highest activity for the degradation of MO (Fig. S4b). A complete decolorization of MO can be achieved with only 30 min. As shown in Fig. 5a, the activity of SZTO-H is even slightly higher than the famous P25 and the reported high efficient ZTO [12]. However, as for SZTO-S and SZTO-H-S, the decolorization of MO requires at least 100 min (Fig. S4c, d). Pristine SnO₂ shows the lowest activity, which is only slightly higher than the photolysis process. Thus, the high activity of SZTO-H which is composed of half ZTO and half SnO_x cannot be simply understood as a one-half of the superposition performance of ZTO and SnO₂.

To quantitatively compare the activity, the degradation kinetic of MO was further analyzed based on the result shown in Fig. 5a. The data was fitted by a pseudo first-order kinetic equation $\ln(C_0/C) = kt$, a model commonly used to describe the degradation of dyes [9,59]. The degradation rate constants (k) then can be obtained according

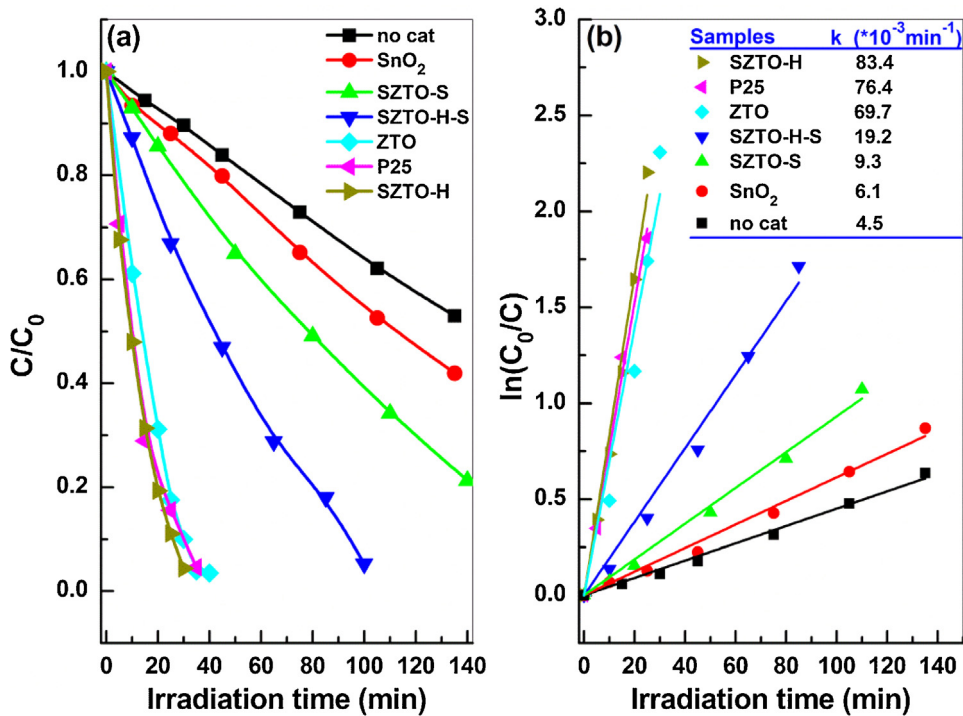


Fig. 5. (a) Kinetic of the degradation of MO over the different photocatalyst. (b) Plots of $\ln(C_0/C)$ against reaction time. C_0 is the initial concentration of MO, C is the concentration after irradiation of t min.

to the lines' slopes. As shown in Fig. 5b, the k value of SZTO-H is as high as $83.4 \times 10^{-3} \text{ min}^{-1}$. The value is much larger than that of SZTO-H-S (19.2×10^{-3}) and SZTO-S (9.3×10^{-3}), and even slightly larger than P25 (76.4×10^{-3}) and ZTO (69.7×10^{-3}). To evaluate the stability of SZTO-H, cycle tests for the degradation of MO were conducted. The catalyst was recovered after each run by centrifugation and then reused in the next cycle in a fresh MO solution. As shown in Fig. S5, although a slight reduction of the degradation efficiency can be found, the decay curves of MO nearly parallel to each other in the tests. The decrease of the efficiency may be caused by the loss of SZTO-H in each run.

Photocatalytical degradation of gaseous benzene, a solid-gas phase photocatalytic reaction, on the prepared SZTO samples was further studied and compared with SnO₂, ZTO, and P25. Blank test indicated that the decomposition of highly stable C₆H₆ cannot be achieved under UVC irradiation without photocatalyst. However, as shown in Fig. 6, the degradation and the mineralization of C₆H₆ can be achieved on the investigated samples. The activity is more significant on SZTO-H, ZTO, and P25 than that on SZTO-H-S, SZTO-S, and SnO₂. A steady degradation of C₆H₆ can be reached after irradiation for ca. 120 min except on ZTO. A sustained increase of C₆H₆ and the drop of CO₂ concentrations can be observed on ZTO (Fig. 6d) suggesting the deactivation of ZTO. The conversion (C%) and mineralization (M%) of C₆H₆ on the photocatalysts were calculated by Eqs. (3) and (4) based on the steady-state profiles shown in Fig. 6. The results are summarized in Table 1. As ZTO is unstable for the degradation of C₆H₆, the average concentration of C₆H₆ (120.6 ppm) and CO₂ (469.5 ppm) were used for the calculations. The results reveal that C% decreases in order of ZTO (51.8) > SZTO-H(23.7) > P25(9.6) > SZTO-H-S(6.7) > SnO₂(4.8) > S-ZTO-S(3.5%), while M% decreases in order of SZTO-S(94.8) > SnO₂(92.0) > P25(88.5) > SZTO-H(80.3) > SZTO-H-S(79.3) > ZTO (60.4%). A much higher M% is achieved on SZTO-S, SnO₂ and P25 as only minor amount of C₆H₆ is involved in the degradation reaction on these samples. A similar phenomenon has been observed in our previous work [60]. Although ZTO shows the

highest efficiency for C₆H₆ conversion, the mineralization of C₆H₆ is only 60.4%. Consistent with the reported works [42,60], P25 shows low activity for the degradation of gaseous C₆H₆ and the C% of C₆H₆ is only 9.6%.

r_M which reflects the real degradation rate of C₆H₆ (converted to CO₂) was used to compare the activity of the prepared samples. As shown in Fig. 7, for SZTO samples, r_M decreases in order SZTO-H(38.3) > SZTO-H-S(10.7) > SZTO-S(6.7 $\mu\text{mol h}^{-1} \text{g}^{-1}$). SZTO-H prepared by the one-pot hydrothermal method exhibits the highest activity. The rate is quite larger than that of pristine SnO₂ (8.9 $\mu\text{mol h}^{-1} \text{g}^{-1}$) and even two times higher than that of P25 (17.1 $\mu\text{mol h}^{-1} \text{g}^{-1}$), further confirming the advantage of the one-pot hydrothermal method. This facile route can produce a sample with a large surface area (Table 1) and avoids the formation of surface defects, which are encountered in the preparation of SZTO-H-S and SZTO-S due to the high treatment temperature. The mineralization of C₆H₆ on P25 is not as significant as the decoloration of MO and a color change of P25 from white to slight brown has been observed suggesting the deposition of intermediates [42,60]. ZTO shows the highest mineralization rate of C₆H₆ and the average rate is 62.1 $\mu\text{mol h}^{-1} \text{g}^{-1}$. Unfortunately, the high performance cannot sustain for a long time and a gradual deactivation of ZTO can be found in Fig. 6d. It seems that ZTO is an effective component for the decomposition of benzene ring, but quite unstable. The wide band gap energy (3.5 eV) and the large BET surface area of ZTO (Table 1) are responsible for the highest activity, which benefit the capture of C₆H₆ and the subsequent degradation reaction. These features are very important for the degradation of gaseous benzene as the contact time is only 1.8 s. Unlike ZTO, no deactivation of the prepared SZTO samples has been observed (Fig. 6a–c). The deactivation of ZTO seems to be retarded by coupling with SnO₂.

3.5. Discussion of possible photocatalytic mechanism

It is known that the photo-corrosion of ZnO is a serious issue, which leads to the deactivation of ZnO in photocatalysis process

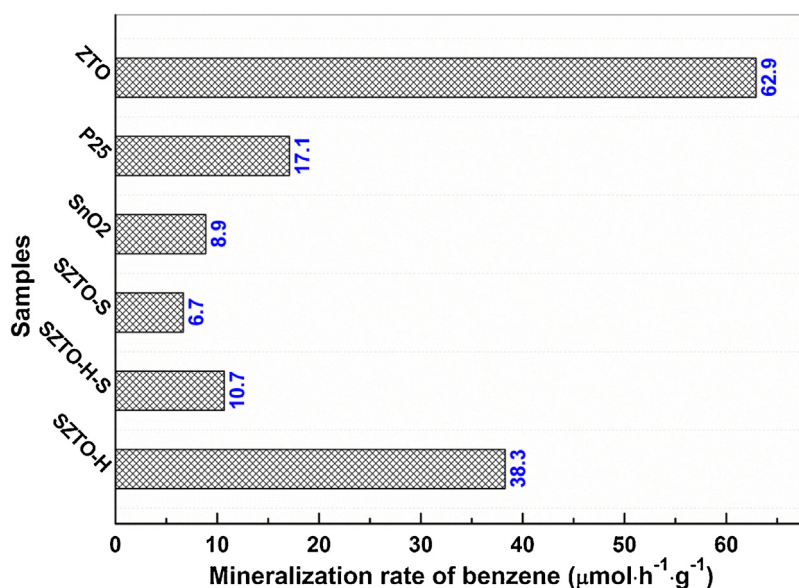
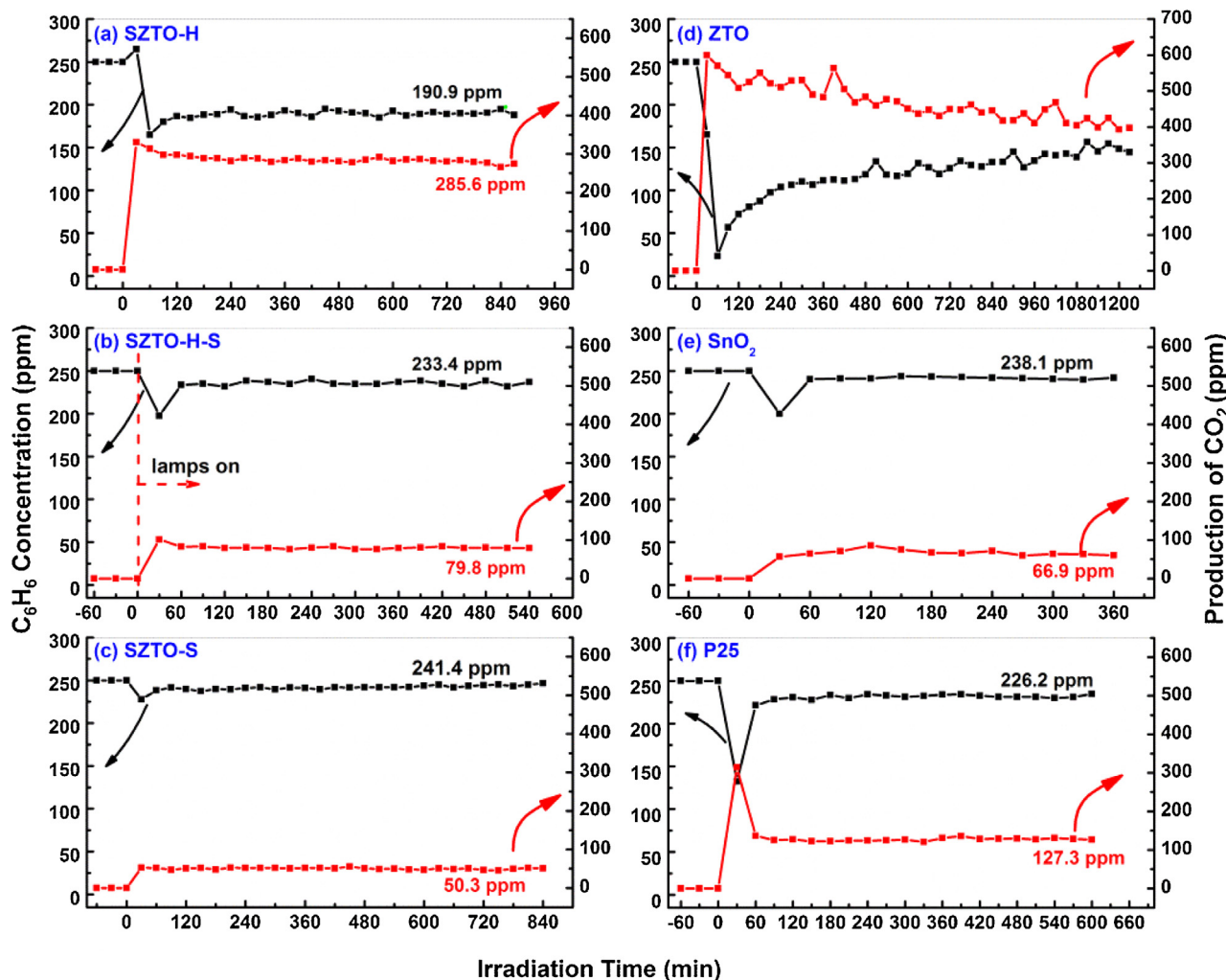


Fig. 7. Mineralization rates of benzene achieved on the SZTO, ZTO, SnO_2 , and P25 samples.

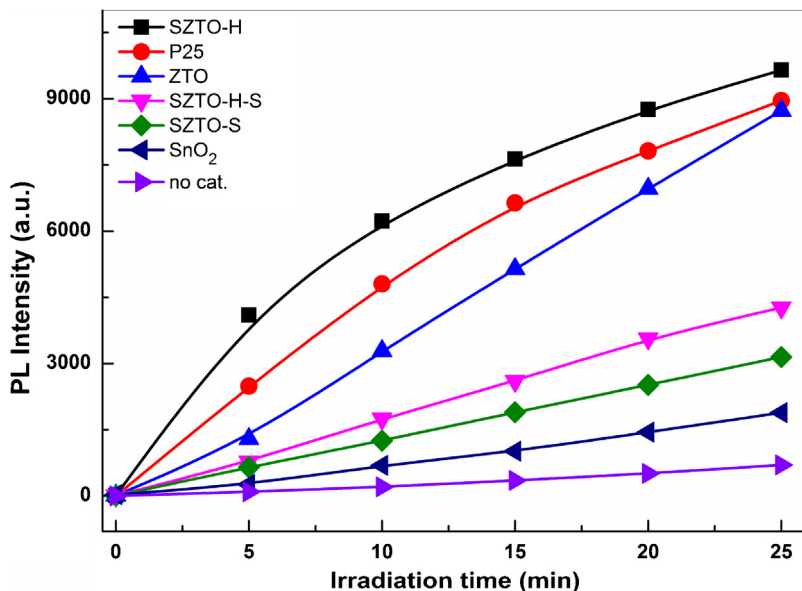


Fig. 8. The fluorescence intensity of TAOH formed with irradiation time in the suspension of the prepared samples and the commercial SnO₂ and P25.

[61]. The reaction is triggered by photo-induced holes (h^+) and can be simply described as $ZnO + 2 h^+ \rightarrow Zn^{2+} + 1/2 O_2$. The decay of ZTO performance may be caused by similar Zn^{2+} elusion. The corrosion of $[ZnO_4]$ tetrahedron or $[ZnO_6]$ octahedron units (denoted as $[ZnO_x]$ for simplicity) in ZTO results in the deactivation. In fact, the damaging of ZTO by the holes also has been suggested in Wu's work [5]. However, we still lack of experimental results to support the assumption. As only 0.1 g sample (mixed with 1 g quartz sands, 50–70 mesh) was used for the degradation of C₆H₆, a further analysis the used sample to confirm the corrosion process is still a technical issue, especially for determining the damage of ZTO microstructure. As the degradation of gaseous C₆H₆ is performed in a water deficient atmosphere, the photo-induced h^+ cannot be effectively captured by surface OH group or adsorbed H₂O. Consequently, the retention time of h^+ in ZTO will be significantly prolonged, which intensifies the corrosion of $[ZnO_x]$ units and makes the deactivation of ZTO more apparent in the degradation of gaseous C₆H₆ than in MO solution.

The stable activity of SZTO-H suggests a transfer of h^+ from ZTO to SnO₂ may be achieved and promoted by the heterojunction formed between SnO₂ and ZTO. The photo-corrosion of $[ZnO_x]$, thus, can be suppressed. However, it should be noted that the transfer of h^+ mainly benefits the stability of ZTO. The activity of SZTO samples is still determined by the intrinsic properties of ZTO and SnO₂ components, such as their surface area, light absorption coefficient, and the separation of e⁻ and h^+ in bulk. Here, as the SZTO samples were prepared by different routes, a careful analysis and quantification of these factors is still hard to be done at present. But, as the active radicals are responsible for the photocatalytic performance, their formation efficiency can objectively reflect the combination effect of these factors and further confirms the optimal preparation route of SZTO. The hydroxyl radical ($\cdot OH$) is an extremely reactive free radical in photocatalytic reaction and the degradation of organic pollutants is generally initiated by $\cdot OH$. The formation of $\cdot OH$ on the investigated photocatalysts was determined by PL technology using TA as a probe molecule. Fig. S6 shows the time-dependent of the PL peak of the product (TAOH). For all tests, the peak intensity increases with the irradiation time suggesting that the formation of TAOH is photo-initiated. SZTO-H, P25, and ZTO show a much higher formation efficiency of TAOH than other samples. The generation of TAOH in the photolysis process (without

any photocatalyst) also can be perceived, which may be formed by the interaction of TA with the dissolved O₂ under UV-C irradiation [42]. But the fluorescence intensity is considerably lower than the tests with photocatalysts.

Theoretically, the TAOH PL peak intensity is in proportion to the amount of photo-induced $\cdot OH$. To compare the formation rate of $\cdot OH$ on the investigated samples, the variation of the PL intensity as a function of illumination time is plotted in Fig. 8. It shows that the TAOH amount increases almost linearly with irradiation time except on SZTO-H and P25. With time prolonged, a retardation of TAOH can be found on the samples. It should be caused by the fact that a large amount of $\cdot OH$ is formed on SZTO-H and P25. In this case, the photo-induced $\cdot OH$ cannot be effectively captured by TA in time due to the short lifetime and the low diffusion rate of $\cdot OH$. Thus, the observed TAOH concentration is actually underestimated [9]. However, for the samples with low formation rates of $\cdot OH$, no such underestimation occurs. Therefore, as shown in Fig. 8, a linear increase of TAOH can be observed on the samples. In general, the formation rates of $\cdot OH$ decreases in order of SZTO-H > P25 > ZTO > SZTO-H-S > SZTO-S > SnO₂, which is consistent well with the photocatalytic performance in the degradation of MO (Fig. 5) and slightly different in the degradation of gaseous C₆H₆. As the TAOH measurements were performed under almost the same conditions as the degradation of MO, a strong correlation between the PL intensity and the decolorization of MO was observed. The result demonstrates that the high efficiency of SZTO-H, P25 and ZTO is due to the efficient production of $\cdot OH$. The low formation rate of TAOH on SZTO-H-S and SZTO-S should be caused by their small surface areas or the surface defects like the oxygen vacancies or Zn interstitials, which can serve as recombination centers of e⁻ and h^+ when excessive of these defects were introduced [62,63].

Among the prepared SZTO samples, only SZTO-H prepared by the one-pot hydrothermal method shows a higher or more stable photocatalytic activity than the pristine ZTO. Considering that SZTO-H shows almost the same absorption coefficient (Fig. 2) and the BET surface area as that of ZTO (Table 1), the stable and high performance of SZTO-H should be benefited by the improved separation of photo-induced charge carriers, which is driven by the heterojunction formed between SnO_x (mainly composed of SnO₂) and ZTO. To confirm this assumption, the transient photocurrents

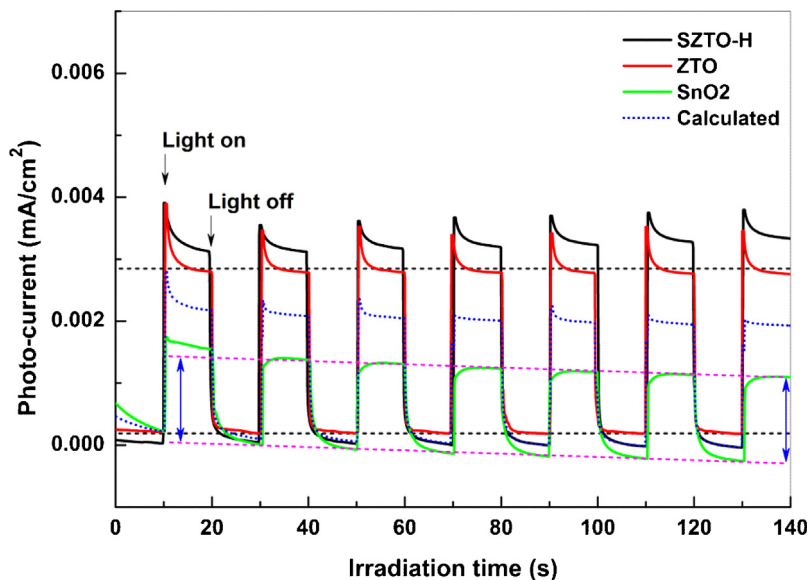


Fig. 9. Transient photocurrent response of the prepared ZTO, SnO_2 , and SZTO-H under 254 nm irradiation. The data labelled as “Calculated” stands for the one-half of the superposition photocurrent of ZTO and SnO_2 .

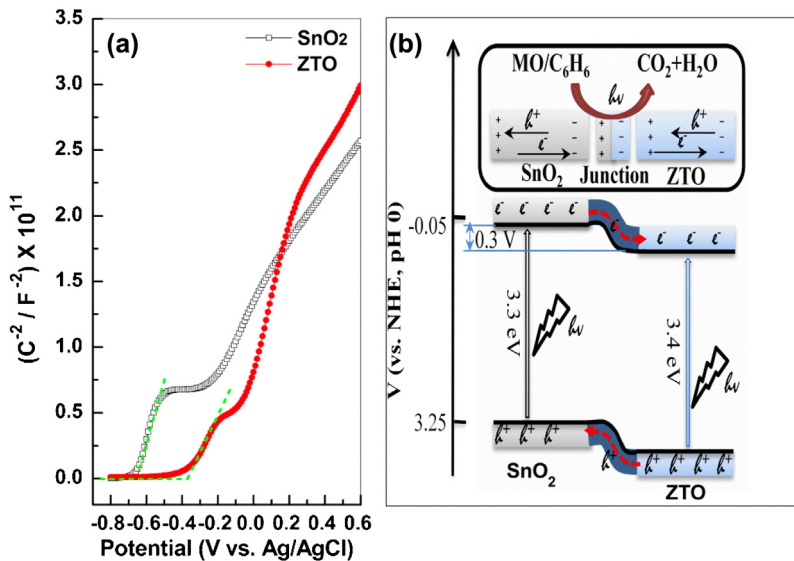


Fig. 10. (a) Mott–Schottky plots for ZTO and SnO_2 ; (b) Schematic illustration of the separation of photo-induced charge carriers at the heterojunction of SnO_2 /ZTO.

generated on ZTO, SnO_2 , and SZTO-H were measured and compared. Attempts to prepare the SnO_x composite have been failed by hydrothermal method. Here, considering that SnO_x is mainly composed of SnO_2 and its XRD diffraction intensity is similar to the pristine SnO_2 , commercial SnO_2 was used as a reference of SnO_x . As shown in Fig. 9, a quick response of the photocurrent can be observed for all tests and the currents are reproducible during several intermittent on-off irradiation cycles. SZTO-H shows the highest photocurrent response and it is about 18% higher than pristine ZTO. If the separation of charge carriers cannot be promoted by the heterojunction, the observed photocurrent of SZTO-H will be the one-half of the superposition photocurrent of ZTO and SnO_2 as SZTO-H is composed of half ZTO and half SnO_x . As indicated by the blue dot line in Fig. 9, the superposition of the half currents is substantially lower than the observed value of SZTO-H, suggesting the function of the heterojunction. A gradual reduction of the photocurrent can be found on ZTO (marked by green dot lines) even the test is only performed for 140 s. However, this phenomenon cannot be

found on SnO_2 and SZTO-H. The responses of SnO_2 located between two parallel lines (denoted by the double arrows in Fig. 9), while the photocurrent on SZTO-H even increases slightly with time. As discussed above, the photo-corrosion of $[\text{ZnO}_x]$ caused by h^+ should account for the reduction of ZTO photocurrent and its low stability. Thus, the stable photocurrent observed on SZTO-H further suggests that a transfer of h^+ from the valence band (VB) of ZTO to the VB of SnO_2 is promoted by the heterojunction.

For composite photocatalysts, the interfacial charge transfer is mainly prompted by their band structures which possess different redox energy levels. Mott–Schottky experiments were performed to investigate the band positions of ZTO and SnO_2 . As shown in Fig. 10a, the positive slopes of the Mott–Schottky plots suggest n-type characteristics semiconductor of SnO_2 and ZTO [6,64,65]. The flat-band potentials (E_{fb}) of SnO_2 and ZTO are estimated to be -0.67 and -0.37 V vs. Ag/AgCl (-0.05 and 0.25 V vs. NHE, pH 0), respectively. The values are close to the reported results [5,66–69]. As the E_{fb} is approximate to the conduction band bottom potential (E_{cb}),

the band structure (Fig. 10b) of the SZTO composite can be constructed based on the information of E_{fb} and E_g of SnO_2 and ZTO. Apparently, the E_{cb} of SnO_2 is more negative than that of ZTO, while the valence band top potential (E_{vb}) of ZTO is more positive than that of SnO_2 . Similar band structure of SZTO composite has been proposed [34,35]. Thus, a type-II heterojunction can be expected. Under irradiation, the photo-induced e^- will transfer from SnO_2 to ZTO due to the energy offset, while for h^+ , a reverse transfer from ZTO to SnO_2 will occur, leading to a wide separation of the charge carriers. Thus, the observed high and stable photocatalytic performance of SZTO-H can be well interpreted by this result, as well as the photocurrent. The transfer of h^+ from ZTO to SnO_2 can be justified by the stability of the SZTO samples, by which the corrosion of ZTO was avoided. The assumption that e^- can transfer from SnO_2 to ZTO is based on two considerations. First, the E_{cb} of SnO_2 is more negative than ZTO. Under irradiation, the photoinduced e^- will be driven from SnO_2 to ZTO by the energy offset. This is a thermodynamic favored process. Second, both SnO_2 and ZTO are N-type semiconductors. The high photo-current of SZTO-H in Fig. 9 suggests that it has more free electrons than pristine ZTO for conduction. The response of SZTO-H is about 18% higher than pristine ZTO, suggesting that a wide separation of photo-induced e^- also could be achieved.

4. Conclusions

A facile one-pot hydrothermal method was developed in this work to synthesize SnO_x/ZTO composite. Characterization results indicate that SnO_x component is SnO_2 accompanied by a trace amount of Sn_2O_3 and a type-II heterojunction can be formed at the interface of SnO_x and ZTO. The heterojunction leads to a wide separation of e^- and h^+ and avoids the corrosion of ZTO by h^+ . Thus, compared to SnO_2 and ZTO, a high and stable photocatalytic performance was observed on SnO_x/ZTO for the degradation of MO and gaseous C_6H_6 . Control tests indicated that, although similar composites could be prepared by the conventional SSR at a high temperature, the activity of the composites is substantially lower than SnO_x/ZTO as some surface defects were introduced into the samples and their surface areas were significantly reduced. This work provides a facile and effective method to fabricate ZTO based composites. Furthermore, we believe that the synthesis strategy has a great potential for the preparation of other ternary oxides based composites, such as $\text{SnO}_x/\text{ZnGa}_2\text{O}_4$ and $\text{SnO}_2/\text{Mg}_2\text{SnO}_4$ [58,70].

Acknowledgements

This work was financially supported by the Natural Science Foundation of China (NSFC, Grant Nos. 21473066, 51472005, and 51272081), the Natural Science Foundation of Anhui Province (Grant Nos. 1408085QB38 and 1608085QB37), and the High Education Revitalization Plan of Anhui Province.

Appendix A. Supplementary data

Supplementary data associated with this article can be found, in the online version, at <http://dx.doi.org/10.1016/j.apcatb.2016.06.070>.

References

- [1] A. Rong, X.P. Gao, G.R. Li, T.Y. Yan, H.Y. Zhu, J.Q. Qu, D.Y. Song, *J. Phys. Chem. B* 110 (2006) 14754–14760.
- [2] I. Stambolova, K. Konstantinov, D. Kovacheva, P. Peshev, T. Donchev, *J. Solid-State Chem.* 128 (1997) 305–309.
- [3] J.H. Yu, G.M. Choi, *Sens. Actuators B-Chem.* 72 (2001) 141–148.
- [4] F. Belliard, P.A. Connor, J.T.S. Irvine, *Solid-State Ion.* 135 (2000) 163–167.
- [5] M.A. Alpuche-Aviles, Y. Wu, *J. Am. Chem. Soc.* 131 (2009) 3216–3224.
- [6] B. Tan, E. Toman, Y. Li, Y. Wu, *J. Am. Chem. Soc.* 129 (2007) 4162–4163.
- [7] L. Zhang, X. Wang, Q. Nong, H. Lin, B. Teng, Y. Zhang, L. Zhao, T. Wu, Y. He, *Appl. Surf. Sci.* 329 (2015) 143–149.
- [8] T. Yan, H. Liu, M. Sun, X. Wang, M. Li, Q. Yan, W. Xu, B. Du, *RSC Adv.* 5 (2015) 10688–10696.
- [9] C.H. Liu, R. Roder, L.C. Zhang, Z. Ren, H.Y. Chen, Z.H. Zhang, C. Ronning, P.X. Gao, *J. Mater. Chem. A* 2 (2014) 4157–4167.
- [10] C. Liu, H. Chen, Z. Ren, S. Dardona, M. Piech, H. Gao, P.-X. Gao, *Appl. Surf. Sci.* 296 (2014) 53–60.
- [11] X.D. Lou, X.H. Jia, H.Q. Xu, S.Z. Liu, Q.H. Gao, *Mat Sci Eng A: Struct.* 432 (2006) 221–225.
- [12] X. Fu, X. Wang, J. Long, Z. Ding, T. Yan, G. Zhang, Z. Zhang, H. Lin, X. Fu, *J. Solid-State Chem.* 182 (2009) 517–524.
- [13] S. Danwittayakul, M. Jaisai, J. Dutta, *Appl. Catal. B* 163 (2015) 1–8.
- [14] W. Cun, Z. Jincai, W. Xinming, M. Bixian, S. Guoying, P. Ping'an, F. Jiamo, *Appl. Catal. B* 39 (2002) 269–279.
- [15] W. Cun, W. Xinming, Z. Jincai, M. Bixian, S. Guoying, P. Ping'an, F. Jiamo, *J. Mater. Sci.* 37 (2002) 2989–2996.
- [16] Z. Li, Y. Zhou, J. Zhang, W. Tu, Q. Liu, T. Yu, Z. Zou, *Cryst. Growth Des.* 12 (2012) 1476–1481.
- [17] H.Y. Chen, J.X. Wang, H.C. Yu, H.X. Yang, S.S. Xie, J.Q. Li, *J. Phys. Chem. B* 109 (2005) 2573–2577.
- [18] H.L. Zhu, D.R. Yang, G.X. Yu, H. Zhang, D.L. Jin, K.H. Yao, *J. Phys. Chem. B* 110 (2006) 7631–7634.
- [19] J.S. Jie, G.Z. Wang, X.H. Han, J.P. Fang, Q.X. Yu, Y. Liao, B. Xu, Q.T. Wang, J.G. Hou, *J. Phys. Chem. B* 108 (2004) 8249–8253.
- [20] J. Fang, A.H. Huang, P.X. Zhu, N.S. Xu, J.Q. Xie, J.S. Chi, S.H. Feng, R.R. Xu, M.M. Wu, *Mater. Res. Bull.* 36 (2001) 1391–1397.
- [21] M.L. Zhang, T.C. An, X.H. Hu, C. Wang, G.Y. Sheng, J.M. Fu, *Appl. Catal. A: Gen.* 260 (2004) 215–222.
- [22] G. Fu, H. Chen, Z.X. Chen, J.X. Zhang, H. Kohler, *Sens. Actuators B: Chem.* 81 (2002) 308–312.
- [23] A. Kurz, K. Brakecha, J. Puetz, M.A. Aegeerter, *Thin Solid Films* 502 (2006) 212–218.
- [24] N. Nikolic, Z. Marinkovic, T. Sreckovic, *J. Mater. Sci.* 39 (2004) 5239–5242.
- [25] S. Baruah, J. Dutta, *Sci. Techn. Adv. Mater.* 12 (2011) 013004.
- [26] J. Zeng, M.D. Xin, K.W. Li, H. Wang, H. Yan, W.J. Zhang, *J. Phys. Chem. C* 112 (2008) 4159–4167.
- [27] L. Shi, Y.M. Dai, *J. Mater. Chem. A* 1 (2013) 12981–12986.
- [28] Y. Zhao, L. Hu, H. Liu, M. Liao, X. Fang, L. Wu, *Sci. Rep.* 4 (2014) 6847.
- [29] D.L. Young, D.L. Williamson, T.J. Coutts, *J. Appl. Phys.* 91 (2002) 1464.
- [30] H. Ullah, A. Khatoon, Z. Akhtar, *Mater. Res. Express* 1 (2014) 045001.
- [31] G.-Z. Zang, X.-F. Wang, L.-B. Li, H.-F. Guo, Q.-D. Chen, *J. Electroceram.* 31 (2013) 134–137.
- [32] M. Slankamenac, I. Ivetic, M.V. Nikolic, N. Ivetic, M. Živanov, V.B. Pavlović, *J. Electron. Mater.* 39 (2010) 447–455.
- [33] R. Liu, W. Du, Q. Chen, F. Gao, C. Wei, J. Sun, Q. Lu, *RSC Adv.* 3 (2013) 2893–2896.
- [34] X.-Y. Liu, H.-W. Zheng, Z.-L. Zhang, X.-S. Liu, R.-Q. Wan, W.-F. Zhang, *J. Mater. Chem.* 21 (2011) 4108–4116.
- [35] T. Jia, J. Zhao, F. Fu, Z. Deng, W. Wang, Z. Fu, F. Meng, *Int. J. Photoenergy* 2014 (2014) 1–7.
- [36] Z.G. Lu, Y.G. Tang, *Mater. Chem. Phys.* 92 (2005) 5–9.
- [37] G.-Z. Zang, H.-H. Liu, J.-F. Lei, X.-F. Wang, L.-B. Li, J.-X. Cao, G.-R. Li, J.A. Varela, *J. Am. Ceram. Soc.* 98 (2015) 2112–2116.
- [38] J.-W. Zhao, L.-R. Qin, L.-D. Zhang, *Solid-State Commun.* 141 (2007) 663–666.
- [39] L.S. Wang, X.Z. Zhang, X. Liao, W.G. Yang, *Nanotechnology* 16 (2005) 2928–2931.
- [40] O.A. Fouad, G. GlasPELL, M.S. El-Shall, *Nano* 05 (2010) 185–194.
- [41] S. Wang, Z. Yang, M. Lu, Y. Zhou, G. Zhou, Z. Qiu, S. Wang, H. Zhang, A. Zhang, *Mater. Lett.* 61 (2007) 3005–3008.
- [42] D. Huang, X. Fu, J. Long, X. Jiang, L. Chang, S. Meng, S. Chen, *Chem. Eng. J.* 269 (2015) 168–179.
- [43] K.-i. Ishibashi, A. Fujishima, T. Watanabe, K. Hashimoto, *Electrochim. Commun.* 2 (2000) 207–210.
- [44] X. Fu, D. Huang, Y. Qin, L. Li, X. Jiang, S. Chen, *Appl. Catal. B* 148–149 (2014) 532–542.
- [45] M.A. Mäki-Jaskari, T.T. Rantala, *Model. Simul. Mater. Sci. Eng.* 12 (2004) 33–41.
- [46] W. Xia, H. Wang, X. Zeng, J. Han, J. Zhu, M. Zhou, S. Wu, *CrystEngComm* 16 (2014) 6841–6847.
- [47] S. Mathur, R. Ganesan, I. Grobelsk, H. Shen, T. Ruegamer, S. Barth, *Adv. Eng. Mater.* 9 (2007) 658–663.
- [48] Y. He, D. Li, J. Chen, Y. Shao, J. Xian, X. Zheng, P. Wang, *RSC Adv.* 4 (2014) 1266–1269.
- [49] G. Chen, S. Ji, Y. Sang, S. Chang, Y. Wang, P. Hao, J. Claverie, H. Liu, G. Yu, *Nanoscale* 7 (2015) 3117–3125.
- [50] J. Tauc, R. Grigorović, A. Vancu, *Phys. Status Solidi B* 15 (1966) 627–637.
- [51] A.K. Sinha, M. Pradhan, S. Sarkar, T. Pal, *Environ. Sci. Technol.* 47 (2013) 2339–2345.
- [52] C.M. Fan, Y. Peng, Q. Zhu, L. Lin, R.X. Wang, A.W. Xu, *J. Phys. Chem. C* 117 (2013) 24157–24166.
- [53] X. Liu, J. Wang, E. Liang, W. Zhang, *Appl. Surf. Sci.* 280 (2013) 556–563.
- [54] H. Zhuang, Q. Gu, J. Long, H. Lin, H. Lin, X. Wang, *RSC Adv.* 4 (2014) 34315–34324.

[55] T. Jia, W. Wang, F. Long, Z. Fu, H. Wang, Q. Zhang, *J. Phys. Chem. C* 113 (2009) 9071–9077.

[56] J.-C. Dupin, D. Gonbeau, P. Vinatier, A. Levasseur, *Phys. Chem. Chem. Phys.* 2 (2000) 1319–1324.

[57] H. Wang, F. Sun, Y. Zhang, L. Li, H. Chen, Q. Wu, J.C. Yu, *J. Mater. Chem.* 20 (2010) 5641–5645.

[58] V.B.R. Boppana, R.F. Lobo, *ACS Catal.* 1 (2011) 923–928.

[59] T. Sauer, G. Cesconeto Neto, H.J. José, R.F.P.M. Moreira, *J. Photoch. Photo. A* 149 (2002) 147–154.

[60] X. Fu, J. Wang, D. Huang, S. Meng, Z. Zhang, L. Li, T. Miao, S. Chen, *ACS Catal.* 6 (2016) 957–968.

[61] L. Zhang, H. Cheng, R. Zong, Y. Zhu, *J. Phys. Chem. C* 113 (2009) 2368–2374.

[62] B. Jiang, Y. Tang, Y. Qu, J.Q. Wang, Y. Xie, C. Tian, W. Zhou, H. Fu, *Nanoscale* 7 (2015) 5035–5045.

[63] H. Kato, A. Kudo, *J. Phys. Chem. B* 106 (2002) 5029–5034.

[64] T. Arai, S. Adachi, *ECS J. Solid-State Sci. Techn.* 1 (2012) R15–R21.

[65] P.P. Das, P. Sujatha Devi, *Inorg. Chem.* 53 (2014) 10797–10799.

[66] T. Kawahara, K. Doushita, H. Tada, *J. Sol-Gel Sci. Techn.* 27 (2003) 301–307.

[67] N. Siedl, S.O. Baumann, M.J. Elser, O. Diwald, *J. Phys. Chem. C* 116 (2012) 22967–22973.

[68] X.P. Lin, F.Q. Huang, J.C. Xing, W.D. Wang, F.F. Xu, *Acta. Mater.* 56 (2008) 2699–2705.

[69] J. Bandara, R.A.S.S. Ranasinghe, *Appl. Cata. A: Gen.* 319 (2007) 58–63.

[70] Y. Qin, J. Xiong, W. Zhang, L. Liu, Y. Cui, H. Gu, *J. Mater. Sci.* 50 (2015) 5865–5872.